

Effects of surface roughness and mineralogy on the sorption of Cm(III) on crystalline rock

Demnitz, M.; Molodtsov, K.; Schymura, S.; Schierz, A.; Müller, K.; Jankovsky, F.;
Havlova, V.; Stumpf, T.; Schmidt, M.;

Originally published:

August 2021

Journal of Hazardous Materials 423(2021)Part A, 127006

DOI: <https://doi.org/10.1016/j.jhazmat.2021.127006>

Perma-Link to Publication Repository of HZDR:

<https://www.hzdr.de/publications/Publ-32811>

Release of the secondary publication
on the basis of the German Copyright Law § 38 Section 4.

CC BY-NC-ND

1 Effects of surface roughness and mineralogy on the sorption of
2 Cm(III) on crystalline rock

3 M. Demnitz,^a K. Molodtsov,^a S. Schymura,^b A. Schierz,^a K. Müller,^a F. Jankovsky,^c
4 V. Havlova,^c T. Stumpf,^a M. Schmidt^{a*}

5
6 ^{a)} *Helmholtz-Zentrum Dresden-Rossendorf e.V., Institute of Resource Ecology, Bautzner
7 Landstraße 400, 01328 Dresden, Germany*

8 ^{b)} *Helmholtz-Zentrum Dresden-Rossendorf e.V., Institute of Resource Ecology, Research Site
9 Leipzig, 04318 Leipzig, Germany*

10 ^{c)} *ÚJV Rez, a.s., Hlavní 130, Rez, 250 68 Husinec, Czech Republic*

11
12 *Corresponding author:

13 Moritz Schmidt

14 email : moritz.schmidt@hzdr.de

15 phone : +49 351 260 3156

16
17 **keywords:** curium; μ TRLFS; crystalline rock; granite; sorption

18
19 **Abstract:**

20 Crystalline rock is one of the host rocks considered for a future deep geological repository for
21 highly active radiotoxic nuclear waste. The safety assessment requires reliable information on
22 the retention behavior of minor actinides. In this work, we applied various spatially resolved
23 techniques to investigate the sorption of Curium onto crystalline rock (granite, gneiss) thin
24 sections from Eibenstock, Germany and Bukov, Czech Republic. We combined Raman-
25 microscopy, calibrated autoradiography and μ TRLFS (*micro-focus time-resolved fluorescence
26 spectroscopy*) with vertical scanning interferometry to study in situ the impact of mineralogy
27 and surface roughness on Cm(III) uptake and molecular speciation on the surface.
28 Heterogeneous sorption of Cm(III) on the surface depends primarily on the mineralogy.
29 However, for the same mineral class sorption uptake and strength of Cm(III) increases with
30 growing surface roughness around surface holes or grain boundaries. When competitive

31 sorption between multiple mineral phases occurs, surface roughness becomes the major
32 retention parameter on low sorption uptake minerals. In high surface roughness areas primarily
33 Cm(III) inner-sphere sorption complexation and surface incorporation are prominent and in
34 select sites formation of stable Cm(III) ternary complexes is observed. Our molecular findings
35 confirm that predictive radionuclide modelling should implement surface roughness as a key
36 parameter in simulations.

37

38 Abbreviations:

39	EPMA:	electron probe micro analysis
40	ISS:	inner-sphere sorption
41	LI:	luminescence intensity
42	LSC:	liquid scintillation counting
43	OSS:	outer-sphere sorption
44	PXRD:	powder x-ray diffraction
45	ROI:	region of interest
46	SF:	surface
47	TRLFM:	time-resolved laser fluorescence microscopy
48	TRLFS:	time-resolved laser-induced fluorescence spectroscopy
49	URF:	Underground Research Facility
50	VSI:	vertical scanning interferometry
51	μ TRLFS:	micro-focus time-resolved laser-induced fluorescence spectroscopy
52	μ XRF:	micro x-ray fluorescence spectrometry

53 1. Introduction

54 The management of highly radioactive waste is one of the major technical and social challenges.
55 Worldwide, underground disposal over the course of hundreds of thousands of years in deep
56 geological repositories is considered to be the safest option for nuclear waste.[1-5] The
57 radioactive waste containers will be surrounded by technical, geoengineered and geological
58 barriers to fulfill safety functions in order to prevent migration of radionuclides towards the
59 biosphere.[6-13] The assessment of safety performance of those barriers is therefore of utmost
60 priority and will depend on reliable and complete thermodynamic data sets and a molecular
61 level understanding of all relevant retention and mobilization mechanisms.

62 Besides salt and clay, crystalline rock is one of the preferred host rock environments considered
63 in many countries, such as Germany or the Czech Republic, for the construction of a nuclear
64 waste repository for high-level radioactive waste.[14-20] This is due to its strong geotechnical
65 stability (and thus facile construction of the repository), low permeability, and low solubility.
66 Crystalline rocks, such as granite, granodiorite, gneiss and other metamorphic rocks, usually
67 consist of a wide set of minerals in varying amounts. However, the most abundant constituents,
68 that are usually present, are quartz, feldspar, and mica. They are accompanied by varying
69 amounts of accessory mineral phases e.g., pyrite, titanite, or prehnite.

70 Several previous studies focused on the sorption of different radionuclides on these individual
71 phases, mainly in the form of mineral powders.[21-33] Using batch sorption experiments
72 information on the retention capabilities of the minerals - ideally by retardation coefficients -
73 with regard to the individual radionuclides were obtained. By combining batch sorption with
74 spectroscopic, microscopic, and quantum chemical approaches details on the retention
75 mechanisms on the molecular scale can be obtained. However, heterogeneous crystalline rocks
76 surfaces are more complex than those of homogeneous mineral powders. On complex multi-
77 mineral surfaces radionuclide sorption behavior is influenced by co-dependencies between
78 mineral phases and heterogeneous surface topographies, especially around mineral grain
79 boundaries.[34-38] Hence, the need arises for an analytical tool capable of deriving molecular
80 level information with sub-mineral grain spatial resolution to visualize and explain inter- and
81 intra-mineral heterogeneities in radionuclide sorption.

82 The highest radiotoxicity in spent nuclear waste, once the short-lived fission products have
83 decayed after ~300 years, can be attributed to the transuranium elements Np, Pu, Am, and
84 Cm.[39, 40] Of these, Am and Cm will be present in their trivalent state. Moreover, Pu maybe
85 also at least partially present as Pu(III) due to the reducing environment encountered in deep

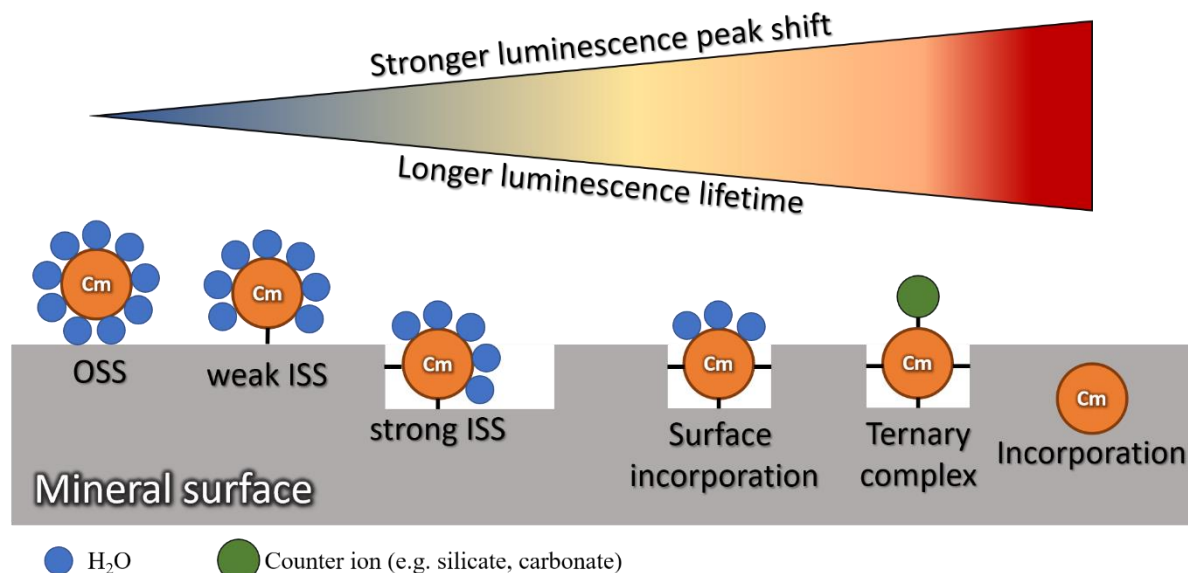
86 geological repositories.[41-45] The actinides Cm, Am, and Pu in their trivalent form exhibit
87 very similar chemical behavior.[46, 47] In this work, we use Cm(III) as a representative of the
88 actinide group mentioned above, which can be used as a molecular probe, because of its
89 excellent luminescence properties. This allows the measurement of Cm(III) concentrations
90 down to approximately $\sim 10^{-12}$ M, that can be considered close to reality in the context of
91 actinide concentrations in a nuclear waste repository.[48]

92 Spectroscopic description of actinide surface sorption

93 Time-resolved laser-induced fluorescence spectroscopy (*TRLFS*) is a convenient method to
94 study the speciation of Cm(III) in aqueous solution and at solid/water interfaces by monitoring
95 its luminescence peaks shifts. Cm(III) emission bands will be bathochromically shifted (“red
96 shift”) when the first coordination shell of the emitting Cm(III) ion changes. The Cm(III) aquo
97 ion luminesces at 593.8 nm,[49] when water molecules in its first hydration shell are substituted
98 by chemical bonds to a mineral surfaces the luminescence signal will be red-shifted
99 ($\lambda_{\text{max}} > 593.8$ nm).[50] The more water molecules are replaced by stronger ligands from the
100 surface or solution, e.g. in the formation of surface incorporation species or ternary surface
101 complexes, the stronger is the observed red-shift. [21, 51] In contrast, Cm(III) bound to the
102 surface with its hydration shell intact will luminesce at the same $\lambda_{\text{max}} = 593.8$ nm as the aquo
103 ion, as its first coordination shell has not changed. [22] Thus, the peak positions of Cm(III)
104 luminescence can be used to distinguish inner-sphere sorption (ISS) complexes, chemically
105 bound to the surface from electrostatically bound, fully hydrated outer-sphere sorption (OSS)
106 complexes (see Figure 1).

107 Additional structural information can be obtained from the time dependent decay of the
108 luminescence. Quenching processes will shorten the luminescence lifetime by providing a non-
109 luminescent pathway for bridging the energy gap between excited and ground state. In the scope
110 of our experiments the most relevant quencher is water, which quenches Cm(III) luminescence
111 by OH-vibrations. Therefore the more water molecules surround the Cm(III) the higher the
112 quenching effect and in turn the shorter the luminescence lifetime. Cm(III) is typically
113 coordinated by nine water molecules in its first coordination sphere, which corresponds to a
114 lifetime of 68 μs .[50] In contrast, complexation of Cm(III) with other ligands (or a mineral
115 surface) that replace water molecules usually leads to longer lifetimes. This correlation is
116 influenced by the presence of other quenching pathways, such as energy transfer to transition
117 metals, e.g., iron, whose presence must be considered when interpreting lifetime data. This
118 means a lifetime analysis can give us structural insight and information about the complexation

119 strengths of Cm(III) and formed species: OSS, weak/strong ISS, surface incorporation, ternary
 120 complexes and total incorporation (see Figure 1). The combination of luminescence spectrum
 121 and lifetime analysis is a well-established method to describe Cm(III) speciation in water and
 122 at mineral-water interfaces.[23, 26, 32, 46, 48, 50, 52-55]



123

124 Figure 1: Simplified scheme for Cm(III) sorption on a mineral surface and the thereby formed complexes. OSS = outer-sphere
 125 sorption; ISS = inner-sphere sorption. Cm(III) species with 9 surrounding water molecules are assigned to be OSS complexes.
 126 Complexes with 7 – 8 / 5 – 6 water molecules are weak/strong ISS species respectively. Cm(III) with only 1 – 4 water molecules
 127 remaining in the first coordination sphere are counted as surface (SF) incorporation species, while no water corresponds to
 128 ternary complexes with carbonate/silicate or complete mineral bulk incorporation.

129 Sorption of trivalent lanthanides and actinides has been studied on individual constituents of
 130 crystalline rock, such as quartz, feldspar, and mica. On quartz sorption of Cm(III) was
 131 investigated using TRLFS in the pH range of 3.8 to 9.5.[50] Starting at pH 4, Cm(III) sorbs
 132 onto the quartz surface as an ISS complex, which then hydrolyzes starting at a pH of 5.5.
 133 Luminescence peak maxima were located at 601.4 and 603.6 nm, with both complexes sharing
 134 a common luminescence lifetime of $123 \pm 10 \mu\text{s}$, which corresponds to five coordinating water
 135 molecules (or OH^- ligands) within their hydration shell. In a recent study sorption of
 136 Ln(III)/Am(III)/Cm(III) on K-feldspar was investigated using batch sorption experiments and
 137 TRLFS.[21] Sorption edge studies ($[\text{M}^{3+}] = 5.2 \cdot 10^{-8} \text{ M} - 10^{-4} \text{ M}$) showed that below pH 5 only
 138 small amounts of trivalent metals sorb on K-feldspar in the form of OSS complexes. Above
 139 pH 5 sorption uptake quickly increases up to pH 7.8 where complete sorption was achieved.
 140 Using TRLFS a total of five different sorbed Cm(III) species were identified: OSS below
 141 pH 4.4, three ISS complexes of varying strength above pH 4.4, and a ternary surface complex
 142 presumably involving silicate at pH exceeding 10.0.

143 To the best of our knowledge no studies of Cm(III) sorption on heterogeneous crystalline rocks
144 are currently available in the literature. However, a few studies on the sorption of trivalent
145 lanthanides on heterogeneous crystalline rocks have been published. Eu(III) is usually used as
146 a chemical analogue for trivalent actinides. Eu(III) sorption ($[Eu] = 1 \mu M$) on granite was
147 quantified in the presence and absence of carbonate.[56] It was shown that the sorption process
148 is independent of carbonate, with Eu(III) sorption starting at pH 3, slowly increasing to around
149 20% at pH 5 from where a steep increase to 100% sorption up to pH 8 was observed. Time-
150 resolved laser fluorescence microscopy (*TRLFM*) was used to study Eu(III) sorption on a
151 granite surface consisting mainly of biotite, plagioclase, K-feldspar, and quartz.[57] Using the
152 spatially-resolved technique it was found that Eu(III) sorbs heterogeneously on the surface.
153 Ishida et al. (2009) proposed that sorption is governed by the feldspar phases, with only little
154 sorption on quartz and biotite, while sorption on all three mineral phases occurs primarily
155 around surface cracks. It was concluded that surface roughness has a major effect on the
156 sorption process.[57]

157 Using micro-focus time-resolved laser-induced fluorescence spectroscopy ($\mu TRLFS$), electron
158 probe micro analysis (*EPMA*), micro X-ray fluorescence spectrometry (μXRF) and
159 autoradiography the sorption of Eu(III) on a granite thin section composed of feldspar, quartz
160 and biotite at pH 8.0 was recently investigated by our group.[38] With autoradiography the
161 sorption uptake on a thin section was assessed showing that sorption on quartz is low with
162 comparatively high sorption uptake on biotite and feldspar mineral grains. $\mu TRLFS$ confirmed
163 the heterogeneous inter-mineral differences in sorption of Eu(III) on the granite surface.
164 Luminescence intensity of Eu(III) was detected in decreasing amounts on feldspar, quartz and
165 biotite in that order. Biotite as a Fe-bearing mineral was found to quench the luminescence of
166 the Eu(III), explaining the deviation from the autoradiography signal that showed sorption
167 amounts similar to feldspar. Additionally, the $\mu TRLFS$ provided sufficient spatial resolution to
168 identify increased sorption uptake in the mineral grain boundary region between feldspar and
169 biotite. Also, on the quartz surface heterogeneous sorption was observed. Sorption is limited to
170 only a few places but binding is strong, indicating sorption to surface sites with limited
171 availability, most likely surface defect sites.[38]

172 We performed a similar Eu(III) sorption study on a gneiss thin section sample at pH 7.5.[58]
173 The gneiss has a more complex mineralogy. It mainly consisted of quartz, feldspar, and
174 amphibole, but contained a large number of minor mineral phases. Autoradiography showed
175 that sorption uptake is highest on chlorite, intermediate on amphibole, and lowest on feldspar
176 and quartz. Chlorite could not be analyzed by $\mu TRLFS$ due to its high Fe content, thus $\mu TRLFS$

177 found the highest amount of Eu(III) sorbed on the minor mineral phase prehnite, while less
178 sorption occurred on feldspar and no signal could be detected on quartz. Surprisingly, the two
179 materials - granite and gneiss - show clearly deviating behavior, despite consisting of the same
180 main constituents. The high sorption uptake on amphibole and prehnite, limits the amount of
181 Eu(III) available for sorption on feldspar and especially quartz. The same process also affects
182 the speciation of Eu(III) at the interface, resulting in the preferential formation of stronger
183 bound Eu(III) surface species on feldspar.

184 Our two prior studies demonstrate that surface topography can lead to variations in the retention
185 behavior. This is most prominent in the case of mineral grain boundaries but also intra-mineral
186 roughness variation that is reflecting different availability of, e.g., kink or defect sites, which
187 can lead to significant sorption heterogeneities. In the previous studies, the topography of the
188 surface was, however, not known, but had to be inferred from differences in Eu(III)'s sorption
189 behavior. In this study we expand the investigation of the sorption behavior of Cm(III) on the
190 same granite and gneiss used in our earlier Eu(III) investigations using Raman-microscopy,
191 autoradiography, and μ TRLFS in combination with vertical scanning interferometry (VSI).
192 Vertical scanning interferometry allows the determination of the surface topography with a
193 vertical spatial resolution in the nanometer range. From this data we derive surface roughness
194 in the form of the S_q parameter, the root mean square deviation of the height data that serves as
195 a suitable proxy for sorption site variations. The mineral phases present on the surface are
196 identified by Raman-microscopy. Sorption uptake of Cm(III) can be determined by
197 autoradiography and partially μ TRLFS, allowing us to compare both methods with each other.
198 Most importantly, μ TRLFS allows us to obtain spatially-resolved Cm(III) speciation
199 information on the molecular level from luminescence spectra and luminescence lifetimes.
200 Because there is no natural Cm background in the mineral phases, data interpretation is
201 expected to be easier than in the case of Eu(III), which is often naturally incorporated in
202 minerals. Furthermore, Cm(III) possesses a higher luminescence yield, which permits use of
203 lower concentrations of Cm(III) at 1 μ M in comparison to Eu(III).

204 This sophisticated combination of techniques allows us to correlate uptake and speciation of
205 Cm(III) on natural rock surfaces with the underlying surface topography at close to realistic
206 conditions.

207 2. Materials and methods

208 2.1 Sample preparation

209 The Eibenstock granite sample was obtained from a former uranium mine in Eibenstock,
210 Germany. The material has been used in a previous Eu(III) sorption study applying μ TRLFS.
211 As described elsewhere the granite mainly consists of quartz, K-feldspar, biotite, and
212 muscovite.[38] In order to be used in batch-sorption experiments with powdered rock samples
213 the specimen were cut down using a Buehler AbrasiMatic 300 abrasive cutter and a Buehler
214 IsoMET low speed saw, ground down using an agate-based Fritsch pulverisette 2 mortar grinder
215 and perpetually sieved using a Retch Vibro sieving setup to obtain grain sizes below 63 μm .
216 Parts of the rock were cut into 28 \times 23 mm slabs, which were embedded in epoxy resin. They
217 were polished down to a thickness of 200 μm , followed by a fine polishing using two sizes of
218 diamond crystals (3 and 1 μm), and finally a chemical silica suspension. Before the sorption
219 experiment, the sample was washed with deionized water (MilliQ, 18.2 M Ω ·cm) and ethanol
220 (95%) followed by 15 min of ultrasonification in deionized water in an ultrasonic bath;
221 subsequently it was washed with deionized water and ethanol again.

222 The Bukov gneiss sample was part of a drill core obtained from the Underground Research
223 Facility Bukov (Bukov URF), Czech Republic and consists mainly of feldspar, amphibole, mica
224 and quartz, as previously described.[58] Powder and thin section samples were produced in the
225 same manner as for the Eibenstock granite.

226 In order to perform sorption edge studies 2 g/L of crystalline rock powder were suspended in
227 MilliQ water. NaCl (Carl Roth GmbH & Co. KG; >99.5%) was used as a background
228 electrolyte to achieve an ionic strength of 0.1 M. The pH of the samples was adjusted to
229 pH = 0.5 – 9.1 using HCl (Carl Roth GmbH & Co. KG; 37%) and NaOH (Carl Roth GmbH &
230 Co. KG; 99%) before adding 5 \cdot 10⁻⁷ M of ²⁴⁸Cm(III) or [¹⁵²Eu]Eu(III). The samples were shaken
231 over several days until an equilibrium condition was reached. For the analysis of Cm(III) and
232 Eu(III) remaining in solution, the samples were centrifuged (4020 \times g) and subsequently a
233 100 μL aliquot of the supernatant of each sample was added into 10 mL Ultima Gold™ for liquid
234 scintillation counting (LSC; HIDEX 300 SL). Afterwards the final pH of the sample was
235 measured. See SI for more details.

236 For Cm(III) sorption experiments on the thin sections a solution containing 10⁻⁶ M Cm(III) at
237 pH 8.0 and I = 0.1 M NaCl was prepared. The low Cm(III) concentration ensures that no
238 precipitation of Cm(III) on the surface due to hydrolysis takes place.[21] The thin section was

239 then placed upside down into the sorption solution in a custom-made sorption cell (see Figure
240 S13 in the SI). The cell was sealed and shaken at least 7 days until equilibrium was reached.
241 The thin section was taken out and washed (pH = 8.0; I = 0.1 M NaCl) to remove excess non-
242 sorbed Cm(III).

243 2.2 Powder X-ray Diffraction

244 Powder X-ray diffraction (*PXRD*) was used to qualitatively determine the bulk mineralogy of
245 both samples. Diffractograms of ground powder samples were measured using a Rigaku
246 MiniFlex 600 with Cu K α ($\lambda = 1.54184 \text{ \AA}$) as its X-ray source. The energy was set to 600 W
247 while measuring in a continuous scan mode. The Rigaku D/teX Ultra Si strip-one dimensional
248 detector was used. The 2θ region between 5.0° and 60.0° was measured with a 0.05° resolution.
249 The determined mineral compositions are averages and the percentages of the composition may
250 vary within the crystalline rock.

251 The quantitative bulk mineral composition of Eibenstock granite was determined using PXRD
252 and reported elsewhere.[38] It consists mainly of quartz (45 wt%), feldspar (42.5 wt%), and
253 mica (11.5 wt%).

254 The quantitative Bukov gneiss bulk mineral composition was determined by PXRD as well and
255 reported elsewhere.[58] It consists mainly of feldspar (45.5 wt%), amphibole (30.3 wt%),
256 quartz (13.5 wt%), mica (9.2 wt%), and biotite (1.5 wt%).

257 2.3 Optical microscopy

258 Transmitted light microscopy images of the entire thin sections were taken using a Leica DM-
259 EP equipped with a Jenoptik Progres Gryphax camera. Additionally, reflected light microscopy
260 images of the regions of interest (ROIs) were photographed using a LabRam Aramis (Horiba)
261 Raman-microscope with a $10\times$ magnification objective.

262 2.4 Raman-microscopy

263 Several regions of interest (ROIs) were chosen via microscopic survey of each thin section
264 sample based on the presence of interesting features such as presumed mineralogy and surface
265 roughness (see Figure 2 a). To determine surface mineralogy the ROIs were measured using a
266 LabRam Aramis (Horiba) Raman-microscope. A 532 nm continuous wave laser at 50 mW was
267 used and the slit and pin-hole diameter were set to 200 and 300 μm , respectively. For each ROI,
268 at least a $1\times 1 \text{ mm}^2$ area was measured using a grid of 15 to 20 μm . The obtained data was

269 treated using a Python-based software developed in-house (pycroTRLFS EVAL, HZDR,
270 Germany) to obtain relevant peak positions, which were then compared to reference mineral
271 spectra from the RRUFF database (see SI Figure S12).[38, 59]

272 2.5 Vertical scanning interferometry

273 Vertical scanning interferometry measurements to determine surface topography were carried
274 out using a Sensofar s neox interferometer with three different Nikon Interferometry objectives
275 DI20x, DI50x and DI100x (see SI Table S1 for specifications and achieved resolutions). The
276 interferometer was run using the white light interferometry mode and the data was evaluated
277 using the SensoMap Premium 7.4 (DigitalSurf). Surface height data with a resolution of 1 nm
278 in z-direction is produced by the software from the interference of the light reflected by the
279 sample surface with a reference beam. Depending on the different optical pathways set by the
280 surface height an interference signal is obtained for every pixel from which the surface height
281 can be derived at the point of maximum modulation of the interference pattern.[60] The surface
282 roughness was characterized using the surface parameter S_q , the root mean square of the height
283 difference. To generate surface roughness maps S_q was calculated for every pixel using a 7×7
284 pixel sliding window.

285 2.6 Autoradiography

286 Autoradiography was used to determine the quantitative sorption uptake of Cm(III) on the thin
287 sections. Absolute concentration values were obtained by calibrating the autoradiography
288 image using activity standards of known Cm(III) concentrations that were exposed to the
289 imaging plate in parallel to the thin section samples. To produce the activity standards droplets
290 of 1 μL of acidic (HCl) solutions containing between 0.2 – 5 μM of Cm(III) with two replicates
291 for each concentration step were pipetted on a glass slide. Using the calibration function of
292 ImageJ the grey value of the autoradiography image was transformed into concentration data,
293 with the integrated density being equal to the amount of substance in pmol and the mean value
294 denoting the concentration in pmol/cm^2 of the projected area (see Figures S10/S11 in SI for
295 autoradiography image calibration).

296 The Cm-loaded thin section was placed on a Storage Phosphor Screen BAS-IP SR 0813 E Super
297 Resolution autoradiography plate separated by a 2.5 μm thick plastic foil to avoid
298 contamination of the autoradiography plate. This setup was pressed tightly together by two
299 plastic plates using screws and kept for one week within a light-proof box. After 7 days of
300 exposure time the plate was read out using an Amersham Typhoon Biomolecular Imager (GE

301 Lifesciences) with a pixel size of 10 μm . Note that this is not equal to the physical resolution
302 of the activity distribution, which is lower due to the isotropic emission and scattering of the
303 alpha radiation, which was additionally shielded by the thin plastic foil.[58]

304 2.7 μTRLFS

305 By applying μTRLFS we are able to gain semi-quantitative information on the Cm(III) sorption
306 uptake and qualitative information on its speciation on the surface. From the luminescence
307 lifetime we can calculate the number of water molecules surrounding Cm(III) and gain insight
308 in its coordination environment from the red shift in the measured spectra. This allows us to
309 use Cm(III) as a probe to determine molecular binding motives.

310 The μTRLFS setup we used has been described previously.[38] The laser pulse energy was set
311 to 20 to 25 μJ . To avoid laser ablation of the surface, the sample was moved out of the laser's
312 focal plane by moving the z-axis of the sample stage 60 μm . This resulted in a laser spot size
313 of around 20 μm . Each $1 \times 1 \text{ mm}^2$ ROI was scanned using a 20 μm grid resulting in 2601
314 luminescence spectra per ROI.

315 The luminescence spectra were evaluated using a Python based software (pycroTRLFS EVAL,
316 HZDR, Germany).[38] Each pixel corresponds to a full luminescence spectrum. An appropriate
317 range for peak integration was chosen, from which a linear background was subtracted, and the
318 intensity was integrated to obtain the total luminescence intensity. The peaks were fit using a
319 Gaussian function to yield the peak maxima, which is used to assess the red shift that is
320 associated with the strength of the complexation as detailed above.

321 Luminescence lifetimes were measured on selected pixels. The fitting of the lifetimes was
322 performed by using mono-, bi-, and triexponential decay functions. An appropriate fit was
323 chosen based on a determination coefficient close(r) to a value of one, while keeping the error
324 range of the lifetimes small. From the lifetimes it is possible to calculate the number of water
325 molecules in Cm(III)'s first coordination sphere using Kimura's equation:[61]

326

$$n(\text{H}_2\text{O}) = \frac{0.65 \text{ ms}}{\tau} - 0.88 \quad (1)$$

327 As no more solution is present during our measurements the samples surface can be considered
328 dry. Therefore, we will interpret species with fully hydrated Cm(III) as OSS complexes, since
329 free Cm(III) aquo ions are only present in solution. Any change in peak position and
330 luminescence lifetime then indicates substitution of water in the first coordination sphere by

331 other ligands. For our experiments these will predominantly stem from the surface and the
332 species can thus be identified as ISS complexes, or even more strongly bound surface species
333 (see section 3.1 and 3.2).

334 3. Results

335 3.1 Sorption of Cm(III) on Eibenstock granite

336 Mineralogy of the Eibenstock granite

337 Optically the Eibenstock thin section consists of three differently colored mineral grain types
338 (see Figure 2 a), which size ranges from hundreds of μm to a few mm. According to the PXRD
339 results (see section 2.2) we could identify the grains as quartz (white), feldspar (black), and
340 mica (brown) as seen in optical microscopy.

341 For a more precise identification of the mineral phases four different regions of interest (ROIs)
342 were investigated using Raman-microscopy (see orange rectangles in Figure 2 a). From the
343 Raman spectra, it was concluded that feldspar and quartz were present on all regions. The mica
344 composition could not be determined conclusively, but the spectra suggest mica is mostly
345 present as muscovite. Topaz, a nesosilicate mineral, was also identified in ROI 2. In Figure 4 a
346 ROI 1 is shown exemplarily. It primarily consists of feldspar, quartz, and mica. Details of the
347 other ROIs are given in the SI (see Figures S3-S5)

348 Surface topography

349 Vertical scanning interferometry (see Figure 2 b, Figure 4 b and Figures S3-S5) revealed
350 distinct topographical surface features for all minerals. Mica surfaces are characterized by
351 elongated cracks and streaks up to several micrometers deep. Feldspar grains feature a multitude
352 of surface pits of about 200 nm depth. Cracks similar in depth to what was seen on mica are
353 found on topaz, however, covering a much larger area than for mica. Quartz surfaces are
354 characterized partially by surface pits of about 200 nm depth. A quantification of these different
355 features by proxy using the surface roughness parameter S_q allows us to rank the minerals
356 according to their average S_q value with the according root mean square error: surface
357 roughness is the highest on topaz with an S_q value of 503 ± 45 nm, followed by mica with
358 111 ± 11 nm and feldspar with 95 ± 6 nm. Quartz showed the lowest S_q value of 75 ± 15 nm.
359 These averaged values correlate with the occurrence and depth of pits and cracks on the
360 different minerals and are the result of significant intra-mineral heterogeneities as they are
361 composed of the very rough pit and crack edges and rather smooth areas in between, or areas
362 with high pit/crack densities and smooth areas without these structural features. While the
363 surface topography of the thin section cannot be taken directly as an analogue for naturally
364 occurring fissure topography, surface sites occurring on topography features of the thin section

365 should also exist in nature. There the surface site concentration might differ, but the thin section
366 allows us to control and semi-quantitatively analyze the sites via surface roughness parameters.

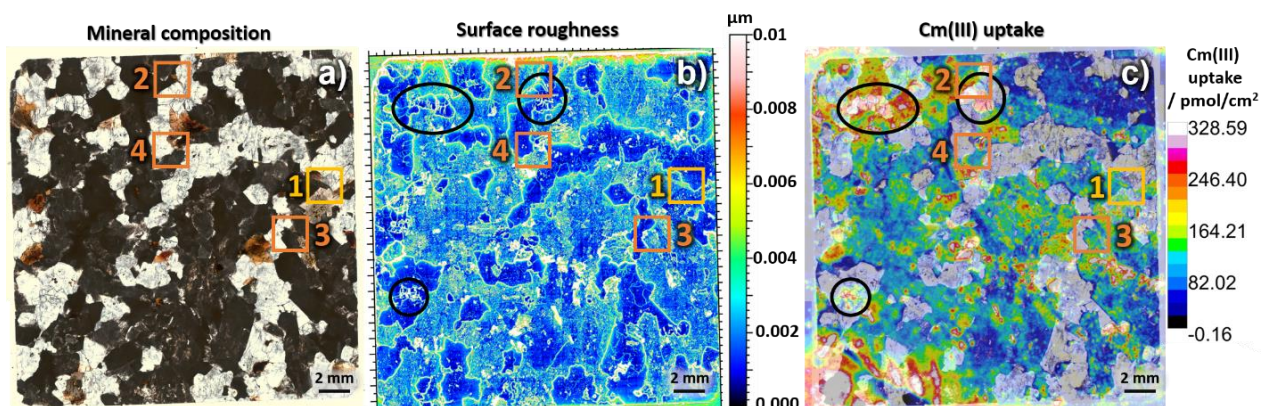
367 In general, the most prominent topographical features besides the mineral textures mentioned
368 above are the grain boundaries. The different resistances of the minerals to the thin section
369 preparation procedures (sawing, polishing, etc.) result in height differences that create distinct
370 features where different mineral grains meet. We find height differences of up to 400 nm
371 between feldspar and quartz and up to 110 nm between feldspar and mica. The quartz/mica
372 grain boundary height difference can reach up to 565 nm. Topaz difference in height to quartz
373 is 175 nm and smaller than the topaz feldspar difference with 416 nm. Again, these height
374 differences as well as the steepness of the grain boundary can be semi-quantitatively
375 characterized using the S_q value. Doing so yields S_q values of up to 80 ± 3 nm for the
376 feldspar/quartz boundary, 15 ± 2 nm for the feldspar/mica boundary, 190 ± 3 nm for the
377 quartz/mica boundary and 108 ± 4 nm and 80 ± 2 nm for the topaz/quartz and topaz/feldspar
378 boundaries, respectively.

379 Sorption uptake of Cm(III)

380 Firstly, sorption was quantified on bulk powder material as a function of pH using Cm(III) for
381 Eibenstock granite. The relative uptake as a function of solution pH can be seen in Figure S1 in
382 the SI: (a) Up to pH 3 no metal uptake from the solution can be observed, (b) from pH 3 to 5.2
383 sorption increases to around 30%. (c) Increasing the pH to 7.5 results in almost complete
384 sorption of Cm(III). (d) Further increasing the pH from 7.5 onward resulted in no changes in
385 sorption uptake. This sorption behavior is typical for trivalent metals on different mineral
386 phases.[24, 27, 31, 62, 63] However, sorption on bulk material does not deliver information on
387 the mechanism of Cm(III) sorption on the mineral surface and no differentiation between
388 individual mineral phases is possible, which is why a spatially-resolved surface investigation
389 of heterogeneous crystalline rock is required. From the sorption edge studies we determined the
390 ideal pH for Cm(III) sorption experiments on the thin-sections to be pH 8.0, since here complete
391 sorption takes place, but bulk precipitation should still be negligible.

392 To locally quantify the Cm(III) sorption uptake on Eibenstock granite (i.e. specific to each
393 mineral phase) we used calibrated autoradiography as shown in Figure 2 c. Cm(III) sorption
394 uptake on Eibenstock granite is quite heterogeneous. When considering each mineral phase
395 separately, uptake decreases as follows: biotite > feldspar ~ topaz > quartz. Similar tendencies
396 are seen for reported log K values in literature for Eu(III), which are directly comparable via
397 the chosen reaction scheme (see SI Table S2). [64, 65] Our autoradiography analysis shows that

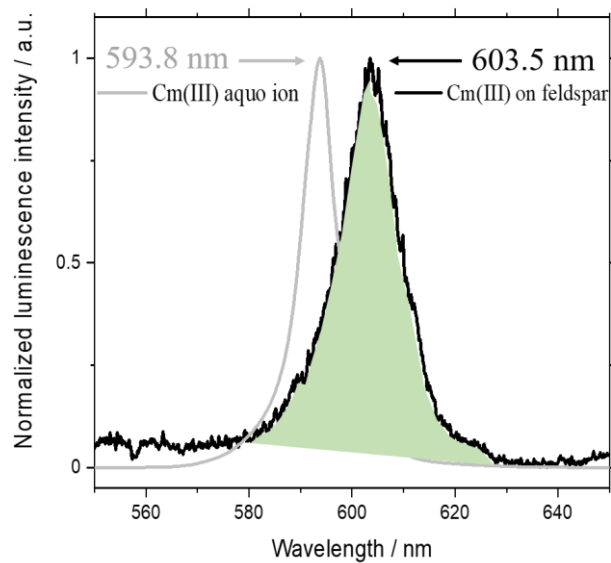
398 sorption occurs mainly on feldspar and biotite mineral grains showing over 300 pmol/cm²
399 sorption uptake, while generally the sorption on quartz mineral grains is below 80 pmol/cm².
400 Only in quartz areas with a higher inherent surface roughness the sorption uptake increases to
401 a similar amount as observed on feldspar and mica (see black ellipses in Figure 2 b, c and
402 Figures S2 – S5). The lower left part of the thin section shows high sorption uptake, which can
403 be traced back to part of the thin section breaking in that area. This had no impact on the
404 following measurements of ROI 1 – 4 but can be considered an artifact. The Cm(III) sorption
405 uptake has now been quantified on each mineral phase, yet the molecular speciation of the
406 sorbed Cm(III) has remained unknown, which is why we applied μ TRLFS.



407

408 Figure 2: a) Optical image of the Eibenstock granite thin section with orange marked ROIs (for detailed ROI analysis see Figure
409 4 and Figure S3 – S5), b) surface roughness determined using interferometry (VSI) and c) Cm(III) sorption uptake determined
410 using quantitative autoradiography. The black ellipses indicate high surface roughness/sorption uptake areas on quartz.

411 Using μ TRLFS we can determine Cm(III) sorption uptake based on the integral luminescence
412 intensity (LI) (see Figure 3 and for integration ranges see Figure 4). More importantly, we can
413 use the measured spectra to characterize Cm(III)'s bond strength to the surface from the
414 observed red shift in comparison to the Cm(III) aquo ion and the number of water molecules
415 remaining in its first coordination sphere from the measured lifetimes. On all ROIs (see Figure
416 3 and Figure S3-S5) we found that the overall distribution of the LI is heterogeneous not only
417 between the different mineral phases, but also within the same mineral grains. LIs were found
418 to be highest on feldspar and topaz, intermediate on quartz and only weak signals were detected
419 on muscovite and other mica (LI ~ 25 : 3 : 1). In contrast, autoradiography showed high sorption
420 uptake on mica. Most likely luminescence quenching takes place here, due to the high Fe
421 content, hindering luminescence detection.

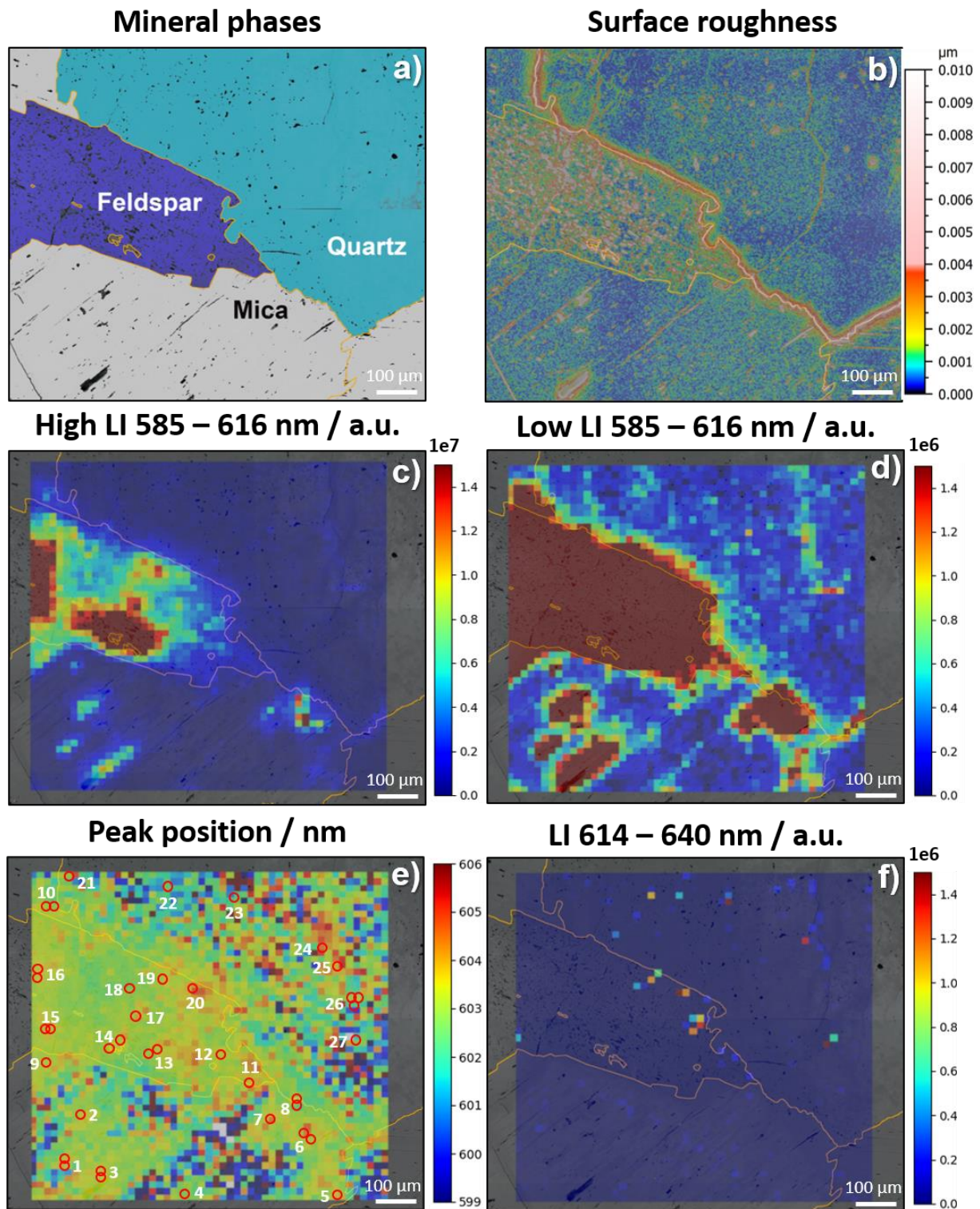


422

423 Figure 3: Exemplary high LI spectrum of Cm(III) sorbed on feldspar (black) and a non-complexed Cm(III) aquo ion in
 424 solution (grey). The peak maxima are indicated by the arrows and the integral luminescence intensity by the green area. The
 425 Cm(III) feldspar spectrum represents one pixel in the measured μ TRLFS maps.

426 Speciation of Cm(III)

427 In the following section and in Figure 4 the focus is set on Cm(III)'s distribution and speciation
 428 in ROI 1 (see Figure 2). Nevertheless, the results of the other ROIs (see SI Figures S3-S5) are
 429 included in the discussion.



430

431 Figure 4: Analysis of ROI 1 on Cm(III) loaded Eibenstock granite: a) mineral composition (Raman-microscopy), b) surface
 432 roughness (S_q ; interferometry), c) high luminescence regime of Cm(III) (μ TRLFS; integral area) and d) the by a factor of 10
 433 decreased scale of the low luminescence regime of Cm(III) (μ TRLFS; integral area), e) by Gaussian peak fitting obtained peak
 434 maxima of the Cm(III) peaks (μ TRLFS; lifetimes measurements spots indicated by red circles) and f) luminescence intensity
 435 of Cm(III) at higher wavelengths (μ TRLFS; integral area).

436 ROI 1 is characterized by feldspar, quartz and mica mineral grains (see Figure 4 a). High surface
 437 roughness areas can be observed around feldspar surface pits, mica cracks, and the mineral
 438 grain boundaries of quartz with both, mica and feldspar (see Figure 4 b).

439 Within ROI 1 we observe that Cm(III) sorption occurs heterogeneously, with the sorption being
440 highest on feldspar, especially in areas with a high surface roughness such as surface pits
441 (compare Figure 4 b and c). When looking at the full range of LIs (see Figure 4 c) all other
442 minerals appear homogeneous and show almost no sorption. A change in scales (see Figure 4 d)
443 reveals that the distribution of Cm(III) is quite heterogeneous also on the other mineral phases,
444 with distinct areas of higher sorption uptake.

445 Gaussian fitting of all Cm(III) luminescence spectra yields a map of the peak maximum in each
446 pixel, which depends on the strength of the ligand field around Cm(III) and thus gives an
447 indication of the bond strength to the surface (Figure 4 e).

448 Peak maxima on feldspar are located between 602 and 605 nm, indicating that ISS complexes
449 of varying strength have formed. An additional strongly red-shifted Cm(III) peak can be
450 detected at selected spots on feldspar, which also occurs on quartz and their grain boundary
451 with each other (see Figure 4 f). On feldspar and the grain boundaries of feldspar and quartz
452 this peak maximum is located between 621 and 625 nm. Cm(III) signals at wavelengths that
453 clearly exceed 620 nm are typically incorporated species, red shifts of ternary complexes on a
454 mineral surface are similar but typically less pronounced.[23, 66-70] Structural incorporation,
455 however, appears unlikely, since the experiment time of just one week seems too low for
456 Cm(III) incorporation into feldspar to take place.[71]

457 On quartz, sorption heterogeneity is only revealed when reducing the luminescence intensity
458 scale by a factor of ten (Figure 4 d). In general, low levels of sorption are observed on quartz,
459 occurring mainly in areas with increased surface roughness, especially at quartz' grain
460 boundary with mica. Some low roughness areas on quartz had such a low LI that no peak fitting
461 was possible. In areas with higher LI we observed peak maxima between 602 and 605 nm,
462 showing the formation of ISS complexes with varying bond strength similar to feldspar. We
463 also observed strongly red-shifted peaks at 625 – 630 nm on quartz, even more strongly shifted
464 than similar features on feldspar, which would again indicate incorporation or ternary complex
465 formation (see Figure 4 f). Such strong luminescence shifts exceeding 620 nm as we observe
466 here on feldspar and quartz are typically associated with Cm(III) structurally incorporated into
467 crystalline materials.[23, 66, 67, 70] However, our experimental procedure, in particular the
468 short reaction time of only 7 d makes it appear unlikely that such a process could have occurred.
469 The only other species which exhibit similar, albeit typically lower peak shifts (~610+ nm) are
470 ternary surface complexes, which could here have formed by partial dissolution of a mineral to
471 provide e.g. SiO_4^{4-} as a co-ligand. It remains unclear, why the ternary complexes would exhibit

472 such extraordinarily large red shifts, or how an incorporation process could occur in such a
473 short time and our data do not allow an unambiguous identification. A possible explanation is
474 the formation of a ternary complex from a SF incorporation species with an already high
475 coordination number from the surface (see Figure 1) in which the ligand from solution
476 completes the coordination shell. Of course, such a species could also be considered as an
477 incorporation species.

478 Generally, the LI on mica outside of areas with a high surface roughness - such as the surface
479 cracks - is low, due to Fe quenching the luminescence[72] since high sorption uptake was seen
480 in autoradiographic measurements. Peak maxima on mica range from 603 to 604 nm, indicating
481 a more homogeneous distribution of ISS complexes.

482 On topaz found on ROI 2 (see Figure S3) we obtained high intensity signals close to mineral
483 boundaries and cracks with peak maxima ranging from 599 to 601 nm, suggesting weaker ISS.
484 In contrast smoother regions show comparatively lower LI, but stronger ISS with peak maxima
485 of 601 up to 604 nm.

486 Luminescence lifetime measurements allow the determination of the detailed speciation of
487 Cm(III) sorbed to the mineral surface by calculating the number of water molecules in the
488 coordination sphere of the Cm(III). In summary, 137 individual lifetime measurements (see
489 Table S3) were performed for all ROIs at different points as indicated by circles in Figure 4 e
490 for ROI 1 and Figure S3 – S5 for ROIs 2 – 4. The points were chosen and evaluated depending
491 on their surface roughness (smooth/rough) and proximity to mineral grain boundaries. In order
492 to obtain a better differentiation between the formed species we categorized them: Cm(III)
493 species with 9 surrounding water molecules are assigned to be OSS complexes. Complexes
494 with 7 – 8 and 5 – 6 water molecules are weak and strong ISS species, respectively. Cm(III)
495 with only 1 – 4 water molecules remaining in the first coordination sphere are identified as
496 surface (SF) incorporation species, while no water corresponds to ternary complex formation
497 with carbonate/silicate or complete mineral bulk incorporation. For a visual representation the
498 reader is referred to Figure 1. The results of these measurements are listed in Table 1 sorted
499 according to their mineral phases and surface roughness.

500 Table 1: Summary of measured lifetimes on all regions of interest on Eibenstock granite corresponding to mineral form and its
501 topography features (ISS = inner-sphere sorption, OSS = outer-sphere sorption, SF = surface). For details the reader is referred
502 to section 3.1. The error 0.5 for calculated water molecules originates from the (1) Kimura equation if only few data points or
503 data points of the exact same value exist. For data sets with multiple data points the error was calculated by applying simple
504 standard deviation. Smooth and rough surfaces were determined by visual inspection of the S_q distribution maps.

Mineral form	n(H ₂ O)	Species
Feldspar (smooth)	7.4 ± 0.5	Weak ISS (23%)

	5.7 ± 0.5	Strong ISS (47%)
	3.3 ± 0.7	SF incorporation (30%)
Feldspar (rough)	9.0 ± 0.5	OSS (5%)
	7.5 ± 0.5	Weak ISS (6%)
	5.1 ± 0.3	Strong ISS (26%)
	3.4 ± 0.8	SF incorporation (63%)
	0.0 ± 0.5	Ternary complex/ Bulk incorporation
Feldspar/Mica*	9.0 ± 0.5	OSS
	7.0 ± 0.5	Weak ISS
	5.7 ± 0.5	Strong ISS
	3.0 ± 0.8	SF incorporation
Quartz (smooth)	5.5 ± 0.5	Strong ISS
	3.0 ± 1.0	SF incorporation
Quartz (rough)	5.7 ± 0.5	Strong ISS
	0.0 ± 0.5	Ternary complex/ Bulk incorporation
Quartz/Feldspar	5.0 ± 0.5	Strong ISS
	3.5 ± 0.5	SF incorporation
Quartz/Mica*	9.0 ± 0.5	OSS
	7.5 ± 0.5	Weak ISS
	6.0 ± 0.5	Strong ISS
	3.0 ± 0.5	SF incorporation
Topaz (smooth)	4.0 ± 0.5	SF incorporation
Topaz (rough)	6.0 ± 0.5	Strong ISS
	2.8 ± 1.6	SF incorporation
Mica (smooth)*	9.0 ± 0.5	OSS
	7.0 ± 0.5	Weak ISS
	6.0 ± 0.5	Strong ISS
	3.0 ± 1.0	SF incorporation
Mica (rough)*	7.5 ± 0.5	Weak ISS
	5.0 ± 0.5	Strong ISS

	3.0 ± 1.0	SF incorporation
--	-----------	------------------

505 *mineral phases containing Fe; where Fe quenching occurs equation (1) is no longer applicable, and the number of coordinating water
506 molecules would be lower than given here

507 Most lifetime points were measured on feldspar grains, which is why the analysis for feldspar
508 is the most reliable. Feldspar mineral grains with a low surface roughness primarily form strong
509 ISS complexes, but surface incorporation and weak ISS complexes also occur. Surface
510 incorporation seems to become the main retention mechanism, along with strong ISS complexes
511 where surface roughness is high. Weak ISS and OSS also occur, primarily in areas where a high
512 sorption uptake can be observed. At feldspar/mica grain boundaries ISS complexes of varying
513 strength as well as OSS complexes are formed. On pixels, where we observed the high red-shift
514 of the above described ternary complex formation or complete incorporation, long
515 luminescence lifetimes for a secondary species were measured, showing that no more water
516 remains in Cm(III)'s hydration shell.

517 On quartz mineral grains strong ISS complexes are found on areas with both low and high
518 surface roughness. Surface incorporation took place mainly on smoother quartz surfaces, while
519 ternary complex formation was more likely to occur on rougher quartz surfaces such as surface
520 pits. As with feldspar ternary complexes/incorporated species on quartz show no more water
521 coordinating Cm(III). Along the quartz grain boundaries to feldspar and mica surface
522 incorporation and strong ISS could be seen.

523 Unfortunately, for mica a detailed lifetime analysis is not useful due to Fe quenching.

524 Topaz mineral grains with a low surface roughness show SF incorporation of Cm(III), while on
525 areas with a higher surface roughness (surface cracks and mineral boundaries) strong ISS
526 complexes occurred additionally.

527 3.2 Sorption of Cm(III) on Bukov gneiss

528 Mineralogy of the Bukov gneiss

529 Visual inspection of the Bukov gneiss thin section reveals smaller (ten to a few hundred μm)
530 and more diverse mineral grains than for the Eibenstock granite (see Figure 5 a). The PXRD
531 results confirmed this optical assessment, and we identify the minerals as quartz (white),
532 feldspar (grey), amphibole (black) and mica (dark-green), with amphibole and mica being
533 associated with each other.

534 For an exact determination of the minerals located on the surface, Raman-microscopy was used
535 (see SI Figure S11 for selected spectra) to investigate four different ROIs (see Figure 5 and
536 Figure S7 – S9). Feldspar, amphibole and quartz were found in each area, while phases such as
537 chlorite (ROI 2), titanite (ROI 2), mica (ROI 3), or pyrite (ROI 4) could only be observed in
538 individual areas. Raman-spectra for amphibole, chlorite, and mica are quite similar, but the
539 phases can be distinguished optically. Chlorite was identified by its needle-like structure, while
540 amphibole and mica have different appearances, looking more smooth or rough, respectively.
541 ROI 1 shown in Figure 6 a) consists primarily of amphibole, quartz and feldspar.

542 Surface topography

543 Using vertical scanning interferometry, the surface topography of the thin section sample was
544 measured and S_q maps (see Figure 5 b) were generated in order to quantify the surface
545 variations. Figure 6 b shows the surface roughness of ROI 1 (see Figures S7 – S9 for
546 ROIs 2 – 4). The surface roughness parameter S_q determined in ROI 1 is lowest on quartz
547 (69 ± 16 nm), intermediate on feldspar (110 ± 12 nm) and highest on amphibole (141 ± 34 nm),
548 very similar to what we found for Eibenstock granite. As with the Eibenstock granite those are
549 average S_q values resulting from areas exhibiting high surface roughness around pits and cracks
550 and smooth areas between those features.

551 Amphibole surfaces are characterized by deep surface cracks of up to $1.3 \mu\text{m}$. Similar to the
552 Eibenstock sample the feldspar surfaces exhibit surface pits, however at larger depth of up to
553 590 nm. Singular surface pits located in quartz can reach depths of $1.1 \mu\text{m}$, but otherwise the
554 surface is the smoothest.

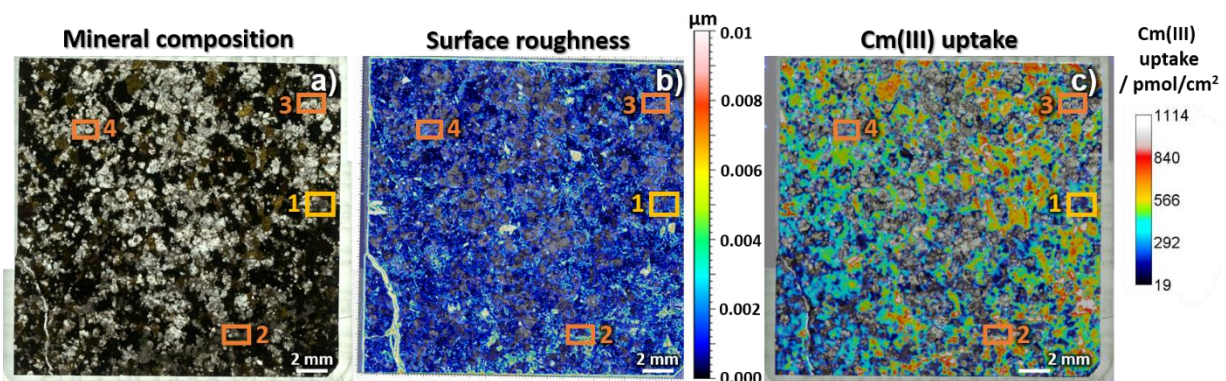
555 The grain boundaries are distinctly visible in the roughness maps with height differences of up
556 to 140 nm between feldspar and amphibole leading to S_q values at a maximum of 123 ± 68 nm.
557 The height difference and surface roughness ($\Delta h = 545$ nm; $S_q = 140 \pm 7$ nm) of the
558 quartz/amphibole grain boundary are larger in comparison to the quartz/feldspar grain boundary
559 ($\Delta h = 375$ nm; $S_q = 31 \pm 22$ nm).

560 Sorption uptake of Eu(III)/Cm(III)

561 Sorption on bulk powder material of Bukov gneiss was quantified as a function of pH using a
562 $5 \cdot 10^{-7}$ M Eu(III) solution spiked with 70 Bq (135 pmol) of ^{152}Eu . Eu(III) was here used as an
563 analogue for Cm(III). The relative uptake as a function of pH of Eu(III) and Cm(III) is near
564 identical for both trivalent metals on the two rocks as seen in Figure S1. (a) Up to pH 3 no metal
565 uptake from the solution can be observed, while (b) from pH 3 to 5.2 sorption increases to

566 around 20%. (c) Complete sorption is reached at pH 7.5 (d) with no further changes in sorption
567 uptake occurring at higher pH. As previously described for Eibenstock granite, we then proceed
568 to quantify the sorption uptake and characterize the speciation of Cm(III) spatially-resolved on
569 the individual mineral phases.

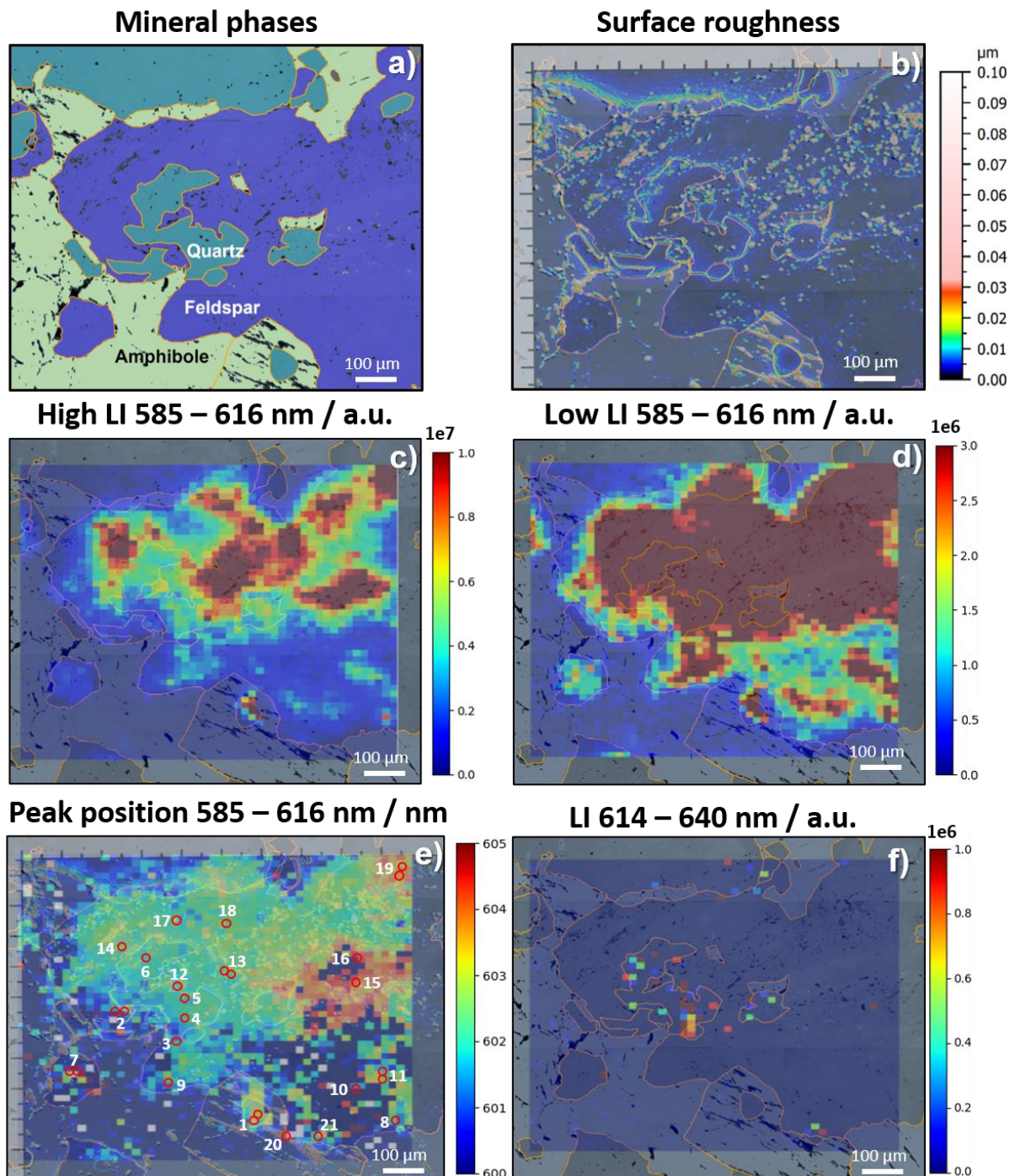
570 Calibrated autoradiography shows highest sorption uptake of Cm(III) on amphibole and mica
571 (see Figure 5 c and Figures S6 – S9) corresponding to 300 – 1100 pmol/cm². This is
572 significantly higher than on Eibenstock granite (~ 330 pmol/cm²). At the same time, Cm(III)
573 uptake on feldspar and quartz phases is significantly lower at only 20 – 100 pmol/cm². Overall,
574 the sorption on the thin section can be seen as heterogeneous, partially varying on the same
575 mineral phases by one order of magnitude. Sorption uptake hotspots correlate with increased
576 surface roughness, especially on amphibole and mica (see Figure 5 a and b). A slight decrease
577 of signal is observed from the upper right to the lower left, probably due to a minor tilt of the
578 sample on the autoradiography imaging plate, which had no impact on the following
579 measurements.



581 Figure 5: a) Optical image of the Bukov gneiss thin section, b) surface roughness determined using interferometry and c)
582 Cm(III) sorption uptake determined using quantitative autoradiography.

583 Speciation of Cm(III)

584 The speciation of Cm(III) was again determined using μ TRLFS. Highest Cm(III) LIs were
585 found on feldspar, less on quartz, and almost no signal was detected on amphibole, mica,
586 chlorite, and pyrite. Low signal intensities can again be traced back to Fe quenching, since
587 autoradiography detected high amounts of sorption on mica and amphibole grains. In the
588 following we will discuss the sorption behavior of Cm(III) on ROI 1 in detail (see Figure 6),
589 nevertheless the results of the other ROIs (see Figure S7-S9) will contribute to the discussion.



590

591 Figure 6: Analysis of ROI 1 on Bukov gneiss: a) mineral composition (Raman-microscopy), b) surface roughness (S_q ;
 592 interferometry), c) high luminescence regime of Cm(III) (μ TRLFS; integral area) and d) low luminescence regime of Cm(III)
 593 (μ TRLFS; integral area), e) by Gaussian peak fitting obtained peak maxima of the Cm(III) peaks (μ TRLFS) and
 594 f) luminescence intensity of Cm(III) at higher wavelengths (μ TRLFS; integral area).

595 ROI 1 on Bukov gneiss consists primarily of feldspar, quartz, and amphibole (see Figure 6 a).
 596 Areas with a high surface roughness can be seen around feldspar surface pits, amphibole cracks
 597 and grain boundaries of quartz with feldspar and mica (see Figure 6 b). The surface pits on
 598 feldspar are clustered thus generating areas on feldspar with a high surface roughness, while
 599 the remaining surface is relatively smooth.

600 Similar to our findings for Eibenstock granite, we observe large differences in sorption uptake
 601 on quartz and feldspar (see Figure 6 c). On feldspar it is directly obvious that differences in
 602 uptake are correlated with the measured surface roughness with rougher areas again showing
 603 higher uptake. This is most obvious for the lower right corner of the ROI, which has the lowest
 604 surface roughness of the feldspar grain and also by far the lowest sorption uptake. The same
 605 also occurs on quartz, but we have reduced the LI scale in order to visualize the areas with
 606 increased sorption on quartz (see Figure 6 d). The same map also reveals additional
 607 heterogeneity within the area of low uptake on feldspar.

608 To characterize the speciation of adsorbed Cm(III) the extent of luminescence peak shifting
 609 was determined by applying a Gaussian fit to all luminescence spectra (see Figure 6 e).

610 As on granite Cm(III) luminescence peaks are more red-shifted in feldspar areas with a higher
 611 surface roughness. Here, peak maxima around 603 to 605 nm indicate strong inner-sphere
 612 complexation.[49] In contrast, on smoother feldspar areas, the maxima are located between 602
 613 and 603 nm pointing toward weaker inner-sphere complexation. [21, 49] However,
 614 luminescence intensity was in some areas so low that no fit was possible.

615 On quartz the peak maxima distribution is narrower with peak maxima ranging from 602 –
 616 603 nm, indicating weak inner-sphere sorption.[50] Further, some luminescence spectra on
 617 quartz and in the quartz/feldspar mineral grain boundary exhibit a second Cm(III) peak with a
 618 high red-shift of 623 up to 626 nm (see Figure 6 f). As discussed above, the strong peak shift
 619 corresponds to either ternary-complex formation or mineral bulk incorporation.

620 Once again we combine the spectral information with lifetime measurements to obtain a more
 621 complete picture of Cm(III)'s speciation on Bukov gneiss. In Table 2 the identified species on
 622 each mineral corresponding to the minerals surface roughness or mineral grain boundary on all
 623 investigated regions of interest are listed, which are based on a total of 91 lifetimes
 624 measurements (see Table S4).

625 Table 2: Summary of measured lifetimes on all regions of interest on Bukov gneiss corresponding to mineral form and its
 626 topography features (ISS = inner-sphere sorption, OSS = outer-sphere sorption, SF = surface). For details the reader is referred
 627 to section 3.2. The error 0.5 for calculated water molecules originates from the (1) Kimura equation if only few data points or
 628 data points of the exact same value exist. For data sets with multiple data points the error was calculated by the simple standard
 629 deviation. Smooth and rough surfaces were determined by visual inspection of the S_q distribution maps.

Mineral form	$n(\text{H}_2\text{O})$	Species
Feldspar (smooth)	9.0 ± 0.5	OSS (14%)
	7.2 ± 0.4	Weak ISS (24%)
	5.7 ± 0.5	Strong ISS (33%)

	3.5 ± 0.8	SF incorporation (29%)
Feldspar (rough)	7.3 ± 0.5	Weak ISS (23%)
	5.3 ± 0.4	Strong ISS (31%)
	2.5 ± 1.3	SF incorporation (46%)
Feldspar/ Mica*	9.0 ± 0.5	OSS
	7.0 ± 0.5	Weak ISS
Feldspar/Amphibole*	7.7 ± 0.5	Weak ISS
	5.7 ± 0.5	Strong ISS
Quartz (smooth)	7.5 ± 0.5	Weak ISS
	6.0 ± 0.5	Strong ISS
	3.0 ± 0.5	SF incorporation
Quartz (rough)	3.0 ± 1	SF incorporation
	0.0 ± 0.5	Ternary complex/ Bulk incorporation
Quartz/Feldspar	9.0 ± 0.5	OSS (18%)
	7.3 ± 0.4	Weak ISS (24%)
	5.4 ± 0.5	Strong ISS (29%)
	3.0 ± 0.9	SF incorporation (29%)
Quartz/Amphibole*	8.0 ± 0.5	Weak ISS
	6.0 ± 0.5	Strong ISS
Amphibole*	7.7 ± 0.5	Weak ISS
	6.0 ± 0.5	Strong ISS

630 *mineral phases containing Fe; where Fe quenching occurs equation (1) is no longer applicable, and the number of coordinating water
631 molecules would be lower than given here

632 Most lifetimes measurements were once more taken on feldspar, making the feldspar data
633 analysis most reliable and detailed. On feldspar with a low surface roughness, ISS complexes
634 of all bond strengths are formed. Mainly strong ISS complexes are formed, followed by surface
635 incorporation, and weak ISS, while OSS could also be observed in a few spots. On feldspar
636 with higher surface roughness generally stronger bound complexes are formed, mainly surface
637 incorporation species, but also strong and weak ISS. The feldspar/mica and feldspar/amphibole
638 mineral grain boundaries show similar sorption behavior, showing weak ISS and OSS, but Fe
639 quenching may impact lifetimes here.

640 Quartz areas with low surface roughness show mainly weak and strong ISS and surface
641 incorporation. In comparison rougher quartz areas again show a shift towards more strongly
642 bound complexes, primarily ternary complex formation/mineral incorporation and surface
643 incorporation species. On pixels with Cm(III) ternary complexes/mineral incorporation we
644 measured long lifetimes, showing that no water remains in the hydration sphere, as was also
645 observed on the Eibenstock granite.

646 The quartz/feldspar grain boundaries show ISS complexes of varying strength as well as outer-
647 sphere sorption. Mainly surface incorporation and strong ISS complexes could be observed, but
648 weak ISS or OSS also occur in some spots. Few lifetime spots could be measured along the
649 quartz/amphibole grain boundary, which correspond to intermediate and weak ISS. However,
650 Fe quenching could also be responsible for decreased luminescence lifetimes.

651

652 4. Discussion

653 By using a combination of calibrated autoradiography and μ TRLFS a comprehensive insight
654 into the sorption uptake of Cm(III) on crystalline rock and its molecular mechanisms was
655 obtained. The individual Cm(III) surface species on the different mineral phases of the
656 heterogeneous crystalline rocks could be identified. Sorption uptake is highest on mica and
657 amphibole phases, followed by feldspar, topaz, and quartz. From the shift of the luminescence
658 peaks and the analysis of luminescence lifetimes, the type of surface complex and its strength
659 were derived. ISS complexes of varying strength are formed on nearly all mineral phases, while
660 OSS complexes are formed in regions with very high sorption uptake, likely since here the
661 available surface sites for ISS become saturated. The strength of the formed ISS complexes is
662 lowest on mica. On quartz and feldspar ISS complexes of similar strength are formed. The ISS
663 complexes on quartz show a chemical similarity to each other, while ISS complexes on feldspar
664 display more variability. Ternary complex formation or incorporation of Cm(III) can be seen
665 on quartz, feldspar, and their grain boundary with each other.

666 The use of vertical scanning interferometry allowed us to correlate surface topography with
667 sorption uptake and speciation on the mineral surface. While mineralogy remains the greatest
668 influence on the sorption process, it is evident for both investigated rocks that topography
669 influences the sorption amount and speciation. Rougher structural features may give rise to a
670 locally increased surface area as well as an increase of reactive surface site density and site
671 reactivity due to increased abundance of structural features such as edge/kink sites and surface
672 defects. Following this approach, we could directly confirm that regions exhibiting a higher
673 surface roughness show an overall higher sorption uptake. We also found a shift to stronger
674 bound Cm(III) surface complexes with increasing surface roughness. We can speculate that
675 kink and defect sites, that appear more numerous in high roughness areas, can form more bonds
676 to Cm(III), resulting in more strongly bound Cm(III).

677 On feldspar, mica, and topaz surfaces the sorption uptake of Cm(III) on the same mineral grains
678 varies greatly depending on the surface roughness. For instance, on the same feldspar mineral
679 grain sorption uptake may be almost one order of magnitude higher in areas with high surface
680 roughness than in smooth areas. These differences in uptake are confirmed by the
681 autoradiography data. Regions with higher surface roughness showed an increase in sorption
682 uptake by one to two orders of magnitude, which was especially interesting for rough quartz
683 regions. Rough quartz surfaces showed almost the same sorption uptake as feldspar or mica
684 mineral grains. The same trend holds true for mineral grain boundaries, which generally

685 coincide with areas of high surface roughness. Grain boundaries on Eibenstock granite with a
686 higher surface roughness such as quartz/mica seem to increase the amount of sorption uptake
687 more significantly than a lower roughness grain boundary such as quartz/feldspar. On low
688 roughness mica areas, luminescence detection with μ TRLFS was not possible at all, presumably
689 due to the combination of reduced uptake on the smooth surface and Fe quenching. But along
690 the mica grain boundary with quartz and around cracks in the mica surface the higher surface
691 roughness increased the sorption uptake sufficiently to make luminescence detection possible.
692 Surface topography is clearly an important factor that needs to be taken into account to describe
693 the sorption behavior of Cm(III). Future studies should focus on determining the impact of
694 surface roughness on radionuclide retention semi-quantitatively. This is particularly relevant
695 for predictive transport modelling of contaminants with respect to the safety of future nuclear
696 waste repositories.

697 The differences in sorption behavior on Bukov gneiss and Eibenstock granite are similar to
698 what was previously found for the sorption of Eu(III) on the same rocks.[38, 58] On Eibenstock
699 granite most of the sorption takes place on feldspar and mica. On the larger investigated area in
700 this study we also observed high Cm(III) sorption uptakes on topaz with similar speciation
701 characteristics as on feldspar, likely due to sorption occurring on aluminol binding sites.

702 One particularly interesting species in this context is the ternary surface complex or
703 incorporation species of Cm(III). We observed species with similar characteristics also in our
704 previous studies with Eu(III). As in this study, incorporation seemed unlikely to have occurred
705 in the short reaction time, so the species was identified as “intrinsic Eu(III)”, i.e. Eu(III)
706 incorporated into the minerals upon their formation, thus unrelated to our experiments. In the
707 case of Cm(III) definitely no intrinsic incorporation of the rare, synthetic element is possible,
708 thus the species must have formed during our experiments. The species’ very large red-shift
709 indicates (near) complete replacement of the hydration shell by stronger ligands, which is
710 confirmed by the species’ long luminescence lifetime. Because the reaction time is only seven
711 days and the species only occurs in areas with very high surface roughness, we currently
712 interpret this species as a ternary complex of a surface incorporation species, likely with silicate
713 or carbonate as an additional ligand.

714 On Bukov gneiss these ternary complexes formed mainly along mineral grain boundaries, while
715 on Eibenstock granite ternary complexes additionally formed on rough feldspar and quartz
716 regions. This might be caused by a concentration effect, since relatively more Cm(III) sorbs on
717 Eibenstock feldspar and quartz than on those minerals on Bukov gneiss, where other mineral

718 phases are preferred targets for Cm(III) sorption. Sorption on feldspar and quartz is only
719 observed in regions with a high surface roughness on Bukov gneiss, causing up to two orders
720 of magnitude difference in luminescence intensity on the same mineral grains. When no rough
721 feldspar areas were present in a region of interest, Cm(III) sorption occurs almost entirely along
722 feldspar/quartz mineral grain boundaries, since those exhibit high inherent surface roughness.
723 This means when another mineral phase such as amphibole is the dominating sorption partner,
724 sorption on mineral phases with lower sorption preference is governed by surface roughness.

725 To analyze the entire sorption system of trivalent metal ions on crystalline rocks we compare
726 the Cm(III) results in this study with our previous studies using Eu(III). Findings obtained in
727 the present study compare well with previous Eu(III) studies.[38, 58] However, one major
728 advantage using Cm(III) is its higher luminescence yield allowing μ TRLFS experiments at
729 concentrations down to 1 μ M thereby avoiding precipitation of metal(hydroxides), which was
730 hampering studies with Eu(III) that had to be conducted at significantly higher concentrations
731 of 50 μ M.[58, 62] Further, Cm(III) as a member of the actinides is a radionuclide which will
732 be present in radioactive waste repositories and is also a better analogue to Am(III)/Pu(III) than
733 Eu(III). Nonetheless, we generally found that the speciation of Cm(III) and Eu(III) on both
734 crystalline rocks is similar as was expected, but we were able to distinguish more species on
735 the mineral surface than previously found for Eu(III)[38] by making use of Cm(III)'s higher
736 luminescence sensitivity The necessary higher Eu(III) concentration in previous studies likely
737 lead to more sorption sites becoming saturated, which we avoid at the lower Cm(III)
738 concentration. Therefore, we identified Cm(III) surface incorporation species on feldspar,
739 quartz, and topaz on both crystalline rocks, which was previously only possible for the Bukov
740 gneiss for Eu(III).[58] For lifetime analysis Cm(III) luminescence is also less influenced by
741 naturally occurring incorporated Eu(III), since the emission of the Eu(III) luminescence only
742 barely overlaps with the Cm(III) emission peaks. Further no natural background of Cm(III)
743 exists that would hinder spectral analysis. Eu(III) luminescence peaks also do not exhibit a peak
744 shift due to complexation, but change their peak ratio.[73] Performing the study with Cm(III)
745 instead of Eu(III) therefore allowed us to gain spatially-resolved insight into sorption uptake
746 and speciation at environmentally relevant concentrations.

747

748 5. Conclusions

749 Our results demonstrate that the sorption of radionuclides such as Cm(III) on multi-mineral
750 samples of natural composition can be well described by combining complementary surface
751 investigation techniques. We combined Raman-microscopy, interferometry, autoradiography,
752 and μ TRLFS to illuminate which factors control the retention of radionuclides on a
753 topographically and mineralogically heterogeneous surface. The combination of techniques
754 was applied to two different crystalline rock systems yielding similar results, which
755 demonstrates a general validity and can therefore suggest extrapolation to other systems should
756 be possible. The actinide Cm(III) performs better as a luminescent molecular probe in spatially-
757 resolved sorption studies in comparison to its previously used lanthanide analogue Eu(III),
758 because of the absence of natural background luminescence, its lower detection limit and more
759 straightforward spectral analysis. The use of Cm(III) allowed us to show preferential sorption
760 areas and describe the surface speciation in detail. Correlating the molecular information on
761 Cm(III) speciation with topography data from vertical scanning interferometry showed that
762 surface roughness is one of the major parameters influencing the sorption behavior of trivalent
763 actinides, second only to the rock's mineralogy. With both rock samples and on all minerals a
764 clear trend of higher uptake in regions of higher surface roughness was observed. Remarkably,
765 surface roughness also impacts the strength of Cm(III) binding to the surface, i.e. complexes
766 are stronger where roughness is higher, likely due to higher availability of high density surface
767 sites.

768 Our results directly affect the safety assessment of potential nuclear waste disposal sites.
769 Insights from model studies using powdered material and/or single minerals, while crucial for
770 a fundamental understanding, cannot be applied to more natural systems straightforwardly.
771 Other factors come to control retention such as topography, grain boundary effects, or mineral
772 competition. These effects will have to be considered when upscaling to larger experiments or
773 applying reactive transport models. Derivation of corresponding numerical parameters is the
774 next challenge. To ensure highest safety standards such parameters and their variability need to
775 be taken into consideration for reactive transport modeling of radionuclides for the safety
776 assessments of radioactive waste repository sites.

777 Acknowledgements

778 We want to thank Anja Schleicher and Uwe Diettmann from the department of Anorganic and
779 Isotope Geochemistry, GFZ, for preparing thin sections samples for us.

780 This work has been developed in the frame of the iCross project. We gratefully acknowledge
781 funding provided by the German Federal Ministry of Education and Research (BMBF, Grant
782 02NUK053) and the Helmholtz Association (Grant SO-093). We further acknowledge financial
783 support to S.Schymura by the Helmholtz-Association (Grant PIE-0007) (CROSSING).

784

785 6. Literature

- 786 [1] M.J. Apted, J. Ahn, Geological repository systems for safe disposal of spent nuclear fuels
787 and radioactive waste, Woodhead Publishing, 2017.
- 788 [2] B. Johnson, A. Newman, J. King, Optimizing high-level nuclear waste disposal within a
789 deep geologic repository, *Annals of Operations Research*, 253 (2017) 733-755.
- 790 [3] K.B. Krauskopf, Geology of high-level nuclear waste disposal, *Annual Review of Earth and*
791 *Planetary Sciences*, 16 (1988) 173-200.
- 792 [4] J.-S. Kim, S.-K. Kwon, M. Sanchez, G.-C. Cho, Geological storage of high level nuclear
793 waste, *KSCE Journal of Civil Engineering*, 15 (2011) 721-737.
- 794 [5] S. Altmann, 'Geo'chemical research: a key building block for nuclear waste disposal safety
795 cases, *Journal of Contaminant Hydrology*, 102 (2008) 174-179.
- 796 [6] M. Apted, J. Ahn, Multiple-barrier geological repository design and operation strategies for
797 safe disposal of radioactive materials, in: *Geological Repository Systems for Safe Disposal of*
798 *Spent Nuclear Fuels and Radioactive Waste*, Elsevier, 2010, pp. 3-28.
- 799 [7] B. Ma, L. Charlet, A. Fernandez-Martinez, M. Kang, B. Madé, A review of the retention
800 mechanisms of redox-sensitive radionuclides in multi-barrier systems, *Applied Geochemistry*,
801 100 (2019) 414-431.
- 802 [8] R. Dohrmann, S. Kaufhold, B. Lundqvist, The role of clays for safe storage of nuclear waste,
803 in: *Developments in Clay Science*, Elsevier, 2013, pp. 677-710.
- 804 [9] W. Hummel, J.W. Schneider, Safety of nuclear waste repositories, *CHIMIA International*
805 *Journal for Chemistry*, 59 (2005) 909-915.
- 806 [10] M.O. Schwartz, Modelling groundwater contamination above the Asse 2 medium-level
807 nuclear waste repository, Germany, *Environmental Earth Sciences*, 59 (2009) 277-286.
- 808 [11] M.O. Schwartz, Modelling groundwater contamination above a nuclear waste repository
809 at Gorleben, Germany, *Hydrogeology Journal*, 20 (2012) 533-546.
- 810 [12] X. Cao, L. Hu, J. Wang, J. Wang, Regional groundwater flow assessment in a prospective
811 high-level radioactive waste repository of China, *Water*, 9 (2017) 551.
- 812 [13] S. Joyce, L. Hartley, D. Applegate, J. Hoek, P. Jackson, Multi-scale groundwater flow
813 modeling during temperate climate conditions for the safety assessment of the proposed high-
814 level nuclear waste repository site at Forsmark, Sweden, *Hydrogeology Journal*, 22 (2014)
815 1233-1249.
- 816 [14] P. Oy, Safety case for the disposal of spent nuclear fuel at olkiluoto, in: *Synthesis*, 2012,
817 pp. 460.
- 818 [15] J. Wang, High-level radioactive waste disposal in China: update 2010, *Journal of Rock*
819 *Mechanics and Geotechnical Engineering*, 2 (2010) 1-11.
- 820 [16] N.P. Laverov, S.V. Yudintsev, B.T. Kochkin, V.I. Malkovsky, The Russian strategy of
821 using crystalline rock as a repository for nuclear waste, *Elements*, 12 (2016) 253-256.
- 822 [17] A. Vokal, M. Brezina, H. Kroupova, M. Ligaunova, Development of methods for
823 efficiency assessment of engineered barriers: Radioactive Waste Repository Authority in:
824 *Annual Report 2001*, Nuclear Research Institute Rez, 2001.

825 [18] P.E. Mariner, E.R. Stein, E.A. Kalinina, T. Hadgu, C.F. Jove-Colon, E. Basurto, US
826 Sections Prepared for Future NEA Crystalline Club (CRC) Report on Status of R&D in CRC
827 Countries Investigating Deep Geologic Disposal in Crystalline Rock, in: SAND2018-4566R
828 662612, Sandia National Lab.(SNL-NM), Albuquerque, NM (United States), 2018.

829 [19] O. Däuper, A. von Bernstorff, Gesetz zur Suche und Auswahl eines Standortes für die
830 Endlagerung radioaktiver Abfälle–zugleich ein Vorschlag für die Agenda der „Kommission
831 Lagerung hoch radioaktiver Abfallstoffe“, Zeitschrift für Umweltrecht, (2014) 24-31.

832 [20] Long-term safety for the final repository for spent nuclear fuel at Forsmark. Main report
833 of the SR-Site project, in: SKB-TR--11-01(V.2), Swedish Nuclear Fuel and Waste
834 Management Co., 2011.

835 [21] J. Neumann, H. Brinkmann, S. Britz, J. Lützenkirchen, F. Bok, M. Stockmann, V.
836 Brendler, T. Stumpf, M. Schmidt, A comprehensive study of the sorption mechanism and
837 thermodynamics of f-element sorption onto K-feldspar, Journal of Colloid and Interface
838 Science, 591 (2020) 490-499.

839 [22] T. Stumpf, A. Bauer, F. Coppin, J.I. Kim, Time-Resolved Laser Fluorescence
840 Spectroscopy Study of the Sorption of Cm(III) onto Smectite and Kaolinite, Environmental
841 Science & Technology, 35 (2001) 3691-3694.

842 [23] T. Stumpf, J. Tits, C. Walther, E. Wieland, T. Fanghänel, Uptake of trivalent actinides
843 (curium (III)) by hardened cement paste: a time-resolved laser fluorescence spectroscopy study,
844 Journal of Colloid and Interface Science, 276 (2004) 118-124.

845 [24] T. Kupcik, T. Rabung, J. Lützenkirchen, N. Finck, H. Geckeis, T. Fanghänel, Macroscopic
846 and spectroscopic investigations on Eu(III) and Cm(III) sorption onto bayerite (β -Al(OH)₃)
847 and corundum (α -Al₂O₃), Journal of Colloid and Interface Science, 461 (2016) 215-224.

848 [25] T. Stumpf, T. Rabung, R. Klenze, H. Geckeis, J. Kim, Spectroscopic study of Cm(III)
849 sorption onto γ -alumina, Journal of Colloid and Interface Science, 238 (2001) 219-224.

850 [26] N. Huittinen, T. Rabung, A. Schnurr, M. Hakanen, J. Lehto, H. Geckeis, New insight into
851 Cm(III) interaction with kaolinite – Influence of mineral dissolution, Geochimica et
852 Cosmochimica Acta, 99 (2012) 100-109.

853 [27] E. Tertre, G. Berger, E. Simoni, S. Castet, E. Giffaut, M. Loubet, H. Catalette, Europium
854 retention onto clay minerals from 25 to 150 C: experimental measurements, spectroscopic
855 features and sorption modelling, Geochimica et Cosmochimica Acta, 70 (2006) 4563-4578.

856 [28] T. Rabung, M. Pierret, A. Bauer, H. Geckeis, M. Bradbury, B. Baeyens, Sorption of
857 Eu(III)/Cm(III) on Ca-montmorillonite and Na-illite. Part 1: Batch sorption and time-resolved
858 laser fluorescence spectroscopy experiments, Geochimica et Cosmochimica Acta, 69 (2005)
859 5393-5402.

860 [29] K. Chung, R. Klenze, K. Park, P. Paviet-Hartmann, J. Kim, A study of the surface sorption
861 process of Cm(III) on silica by time-resolved laser fluorescence spectroscopy (I), Radiochimica
862 Acta, 82 (1998) 215-220.

863 [30] N. Huittinen, T. Rabung, J. Lützenkirchen, S. Mitchell, B. Bickmore, J. Lehto, H. Geckeis,
864 Sorption of Cm(III) and Gd(III) onto gibbsite, α -Al(OH)₃: A batch and TRLFS study, Journal
865 of Colloid and Interface Science, 332 (2009) 158-164.

866 [31] A. Schnurr, R. Marsac, T. Rabung, J. Lützenkirchen, H. Geckeis, Sorption of Cm(III) and
867 Eu(III) onto clay minerals under saline conditions: Batch adsorption, laser-fluorescence
868 spectroscopy and modeling, Geochimica et Cosmochimica Acta, 151 (2015) 192-202.

869 [32] A.S. Kar, S. Kumar, B. Tomar, V. Manchanda, Sorption of curium by silica colloids: Effect
870 of humic acid, Journal of Hazardous Materials, 186 (2011) 1961-1965.

871 [33] S. Virtanen, S. Meriläinen, M. Eibl, T. Rabung, J. Lehto, N. Huittinen, Sorption
872 competition and kinetics of trivalent cations (Eu, Y and Cm) on corundum (α -Al₂O₃): a batch
873 sorption and TRLFS study, Applied Geochemistry, 92 (2018) 71-81.

874 [34] G.K. Darbha, T. Schäfer, F. Heberling, A. Lüttge, C. Fischer, Retention of latex colloids
875 on calcite as a function of surface roughness and topography, Langmuir, 26 (2010) 4743-4752.

876 [35] G.K. Darbha, C. Fischer, J. Luetzenkirchen, T. Schäfer, Site-specific retention of colloids
877 at rough rock surfaces, *Environmental Science & Technology*, 46 (2012) 9378-9387.

878 [36] G. Krishna Darbha, C. Fischer, A. Michler, J. Luetzenkirchen, T. Schäfer, F. Heberling,
879 D. Schild, Deposition of latex colloids at rough mineral surfaces: An analogue study using
880 nanopatterned surfaces, *Langmuir*, 28 (2012) 6606-6617.

881 [37] C. Fischer, I. Kurganskaya, T. Schäfer, A. Lüttge, Variability of crystal surface reactivity:
882 what do we know?, *Applied Geochemistry*, 43 (2014) 132-157.

883 [38] K. Molodtsov, S. Schymura, J. Rothe, K. Dardenne, M. Schmidt, Sorption of Eu(III) on
884 Eibenstock granite studied by μ TRLFS: A novel spatially-resolved luminescence-spectroscopic
885 technique, *Scientific Reports*, 9 (2019) 6287.

886 [39] W.J. Weber, Radiation and thermal ageing of nuclear waste glass, *Procedia Materials
887 Science*, 7 (2014) 237-246.

888 [40] J. Veliscek-Carolan, Separation of actinides from spent nuclear fuel: A review, *Journal of
889 Hazardous Materials*, 318 (2016) 266-281.

890 [41] R.C. Ewing, Nuclear waste forms for actinides, *Proceedings of the National Academy of
891 Sciences*, 96 (1999) 3432-3439.

892 [42] W. Weber, R. Ewing, C. Catlow, T.D. De La Rubia, L. Hobbs, C. Kinoshita, A. Motta, M.
893 Nastasi, E. Salje, E. Vance, Radiation effects in crystalline ceramics for the immobilization of
894 high-level nuclear waste and plutonium, *Journal of Materials Research*, 13 (1998) 1434-1484.

895 [43] T. Standish, J. Chen, R. Jacklin, P. Jakupi, S. Ramamurthy, D. Zagidulin, P. Keech, D.
896 Shoosmith, Corrosion of copper-coated steel high level nuclear waste containers under
897 permanent disposal conditions, *Electrochimica Acta*, 211 (2016) 331-342.

898 [44] L. Duro, C. Domènech, M. Grivé, G. Roman-Ross, J. Bruno, K. Källström, Assessment of
899 the evolution of the redox conditions in a low and intermediate level nuclear waste repository
900 (SFR1, Sweden), *Applied Geochemistry*, 49 (2014) 192-205.

901 [45] B. Grambow, Mobile fission and activation products in nuclear waste disposal, *Journal of
902 Contaminant Hydrology*, 102 (2008) 180-186.

903 [46] A. Heller, A. Barkleit, G. Bernhard, Chemical speciation of trivalent actinides and
904 lanthanides in biological fluids: the dominant in vitro binding form of curium (III) and europium
905 (III) in human urine, *Chemical Research in Toxicology*, 24 (2011) 193-203.

906 [47] S. Skanthakumar, M.R. Antonio, R.E. Wilson, L. Soderholm, The curium aqua ion,
907 *Inorganic Chemistry*, 46 (2007) 3485-3491.

908 [48] H. Moll, T. Stumpf, M. Merroun, A. Rossberg, S. Selenska-Pobell, G. Bernhard, Time-
909 resolved laser fluorescence spectroscopy study on the interaction of curium (III) with
910 *Desulfovibrio äspöensis* DSM 10631T, *Environmental Science & Technology*, 38 (2004) 1455-
911 1459.

912 [49] S. Stumpf, T. Stumpf, C. Walther, D. Bosbach, T. Fanghänel, Sorption of Cm(III) onto
913 different Feldspar surfaces: a TRLFS study, *Radiochimica Acta*, 94 (2006) 243-248.

914 [50] S. Stumpf, T. Stumpf, J. Lützenkirchen, C. Walther, T. Fanghänel, Immobilization of
915 trivalent actinides by sorption onto quartz and incorporation into siliceous bulk: Investigations
916 by TRLFS, *Journal of Colloid and Interface Science*, 318 (2008) 5-14.

917 [51] M.M. Fernandes, T. Stumpf, B. Baeyens, C. Walther, M. Bradbury, Spectroscopic
918 Identification of Ternary Cm–Carbonate Surface Complexes, *Environmental Science &
919 Technology*, 44 (2010) 921-927.

920 [52] J.I. Kim, R. Klenze, H. Wimmer, Fluorescence spectroscopy of curium (III) and
921 application, *European Journal of Solid State and Inorganic Chemistry*, 28 (1991) 347-356.

922 [53] T. Fanghänel, J.I. Kim, R. Klenze, Y. Kato, Formation of Cm(III) chloride complexes in
923 CaCl_2 solutions, *Journal of Alloys and Compounds*, 225 (1995) 308-311.

924 [54] M. Lopez-Fernandez, H. Moll, M.L. Merroun, Reversible pH-dependent curium (III)
925 biosorption by the bentonite yeast isolate *Rhodotorula mucilaginosa* BII-R8, *Journal of
926 Hazardous Materials*, 370 (2019) 156-163.

- 927 [55] H. Moll, M. Schmidt, S. Sachs, Curium (III) and europium (III) as luminescence probes
928 for plant cell (*Brassica napus*) interactions with potentially toxic metals, *Journal of Hazardous*
929 *Materials*, 412 (2021) 125251.
- 930 [56] M.-H. Baik, W.-J. Cho, P.-S. Hahn, Effects of speciation and carbonate on the sorption of
931 Eu (III) onto granite, *Environmental Engineering Research*, 9 (2004) 160-167.
- 932 [57] K. Ishida, T. Kimura, T. Saito, S. Tanaka, Adsorption of Eu(III) on a heterogeneous surface
933 studied by time-resolved laser fluorescence microscopy (TRLFM), *Environmental Science &*
934 *Technology*, 43 (2009) 1744-1749.
- 935 [58] K. Molodtsov, M. Demnitz, S. Schymura, F. Jankovský, M. Zuna, V. Havlová, M.
936 Schmidt, Molecular-Level Speciation of Eu(III) Adsorbed on a Migmatized Gneiss As
937 Determined Using μ TRLFS, *Environmental Science & Technology*, 55 (2021) 4871-4879.
- 938 [59] B. Lafuente, R.T. Downs, H. Yang, N. Stone, The power of databases: the RRUFF project,
939 in: *Highlights in Mineralogical Crystallography*, Walter de Gruyter GmbH, 2016, pp. 1-29.
- 940 [60] Y. Wang, F. Xie, S. Ma, L. Dong, Review of surface profile measurement techniques based
941 on optical interferometry, *Optics and Lasers in Engineering*, 93 (2017) 164-170.
- 942 [61] T. Kimura, R. Nagaishi, Y. Kato, Z. Yoshida, Luminescence study on solvation of
943 americium (III), curium (III) and several lanthanide (III) ions in nonaqueous and binary mixed
944 solvents, *Radiochimica Acta*, 89 (2001) 125-130.
- 945 [62] M.J. Kang, P.S. Hahn, Adsorption behavior of aqueous europium on kaolinite under
946 various disposal conditions, *Korean Journal of Chemical Engineering*, 21 (2004) 419-424.
- 947 [63] X. Tan, M. Fang, J. Li, Y. Lu, X. Wang, Adsorption of Eu(III) onto TiO₂: effect of pH,
948 concentration, ionic strength and soil fulvic acid, *Journal of Hazardous Materials*, 168 (2009)
949 458-465.
- 950 [64] S.M. Britz, Europium sorption experiments with muscovite, orthoclase, and quartz:
951 Modeling of surface complexation and reactive transport, Dissertation, Fakultät Architektur,
952 Bauingenieurwesen und Umweltwissenschaften, Technische Universität Carolo-Wilhelmina zu
953 Braunschweig, 2018.
- 954 [65] C. Richter, Sorption of environmentally relevant radionuclides (U(VI), Np(V)) and
955 lanthanides (Nd(III)) on feldspar and mica, Dissertation, School of Science, TU Dresden,
956 Dresden, 2015.
- 957 [66] J. Tits, T. Stumpf, T. Rabung, E. Wieland, T. Fanghänel, Uptake of Cm(III) and Eu(III) by
958 calcium silicate hydrates: a solution chemistry and time-resolved laser fluorescence
959 spectroscopy study, *Environmental Science & Technology*, 37 (2003) 3568-3573.
- 960 [67] J.-M. Wolter, K. Schmeide, N. Huittinen, T. Stumpf, Cm(III) retention by calcium silicate
961 hydrate (CSH) gel and secondary alteration phases in carbonate solutions with high ionic
962 strength: A site-selective TRLFS study, *Scientific Reports*, 9 (2019) 14255.
- 963 [68] T. Rabung, M. Altmaier, V. Neck, T. Fanghänel, A TRLFS study of Cm(III) hydroxide
964 complexes in alkaline CaCl₂ solutions, *Radiochimica Acta*, 96 (2008) 551-560.
- 965 [69] M.d.S.M. Fernandes, Spektroskopische Untersuchungen (TRLFS und XAFS) zur
966 Wechselwirkung von dreiwertigen Lanthaniden und Actiniden mit der Mineralphase Calcit,
967 Dissertation, Natural Sciences, Mathematics, and Computer Sciences, Ruprecht-Karls-
968 Universität, Heidelberg, 2006.
- 969 [70] N. Huittinen, A.C. Scheinost, Y. Ji, P.M. Kowalski, Y. Arinicheva, A. Wilden, S.
970 Neumeier, T. Stumpf, A spectroscopic and computational study of Cm³⁺ incorporation in
971 lanthanide phosphate rhabdophane (LnPO₄ · 0.67 H₂O) and monazite (LnPO₄), *Inorganic*
972 *Chemistry*, 57 (2018) 6252-6265.
- 973 [71] S.E. Hellebrandt, S. Hofmann, N. Jordan, A. Barkleit, M. Schmidt, Incorporation of Eu(III)
974 into calcite under recrystallization conditions, *Scientific Reports*, 6 (2016) 33137.
- 975 [72] S. Hellebrandt, Grenzflächenreaktionen von Actiniden an Muskovit, Dissertation, School
976 of Science, Technische Universität Dresden, Dresden, 2017.

977 [73] K. Binnemans, Interpretation of europium(III) spectra, Coordination Chemistry Reviews,
978 295 (2015) 1-45.

979

980

